

# Size is Everything: Universal Features of Quasar Microlensing with Extended Sources

Michael J. Mortonson<sup>1,2</sup> and Paul L. Schechter

*Department of Physics, Massachusetts Institute of Technology, 77 Massachusetts Avenue, Cambridge, MA 02139*

and

Joachim Wambsganss

*Universität Potsdam, Institut für Physik, Am Neuen Palais 10, 14467 Potsdam, Germany*

## ABSTRACT

We examine the effect that the shape of the source brightness profile has on the magnitude fluctuations of images in quasar lens systems due to microlensing. We do this by convolving a variety of accretion disk models (including Gaussian disks, uniform disks, “cones,” and a Shakura-Sunyaev thermal model) with two magnification maps in the source plane, one with convergence  $\kappa = 0.4$  and shear  $\gamma = 0.4$  (positive parity), and the other with  $\kappa = \gamma = 0.6$  (negative parity). By looking at magnification histograms of the convolutions and using chi-squared tests to determine the number of observations that would be necessary to distinguish histograms associated with different disk models, we find that, for circular disk models, the microlensing fluctuations are relatively insensitive to all properties of the models except the half-light radius of the disk.

*Subject headings:* gravitational lensing — quasars: general — accretion disks

## 1. INTRODUCTION

The deflection angles associated with gravitational microlensing, due to stellar-mass objects such as stars in a lensing galaxy, are on the order of 1 microarcsecond, too small

---

<sup>1</sup>[mjmort@uchicago.edu](mailto:mjmort@uchicago.edu)

<sup>2</sup>present address: Department of Physics, University of Chicago, 5640 S. Ellis Avenue, Chicago, IL 60637

to be resolved into separate microimages. However, microlensing can have significant effects on the magnitudes of macroimages. Magnitude fluctuations from microlensing have been observed in several lensed quasars. These effects were first observed by Irwin et al. (1989) in the quasar Q2237+0305. This quasar has been recently monitored as part of the Optical Gravitational Lensing Experiment (OGLE), and microlensing fluctuations with amplitudes up to 0.65 magnitudes have been observed (Woźniak et al. 2000a,b). Microlensing can be distinguished from intrinsic quasar time-variability by looking for fluctuations that are uncorrelated between the macroimage light curves. Quasar microlensing could help explain observed flux ratio anomalies for quasars in which the magnitude differences between the macroimages differ greatly from those predicted by theory (Witt et al. 1995; Metcalf & Madau 2001; Chiba 2002; Dalal & Kochanek 2002; Schechter & Wambsganss 2002).

There is a large number of parameters that could be important for modeling lens systems: properties of the source, including its size and shape; lens properties such as the mass distribution of objects that make up the lens; and cosmological parameters like the Hubble constant. Although we expect all of these properties to affect the physics of lensing in some way, the effects of some properties are more significant than the effects of others. It is important to find out which parameters have little effect on the observables in lensing so that those properties can be neglected in lens models.

For quasar microlensing, there is a great deal of evidence that the size of the source has a large effect on the fluctuations due to microlensing. Observations of extragalactic microlensing have been used to place constraints on the sizes of quasars and on the scales over which different quasar emission mechanisms operate (e.g., Wyithe et al. 2000a; Yonehara 2001; Shalyapin et al. 2002; Wyithe et al. 2002; Schechter et al. 2003). A large extended source covers more microlensing caustics in the source plane at a single time than a small source, so its brightness varies less as it moves relative to the lens and observer. As a general rule, the variability of a lensed source will only be significantly affected by microlensing if the source is smaller than the projection of the Einstein radius of a microlens into the source plane (Courbin et al. 2002). (Note, however, that Refsdal & Stabell (1997) have argued that in some circumstances, even relatively large sources can have significant fluctuations due to microlensing.)

The same effect could be responsible for differences between emission-line and continuum flux ratios, which have been found in a number of lens systems (e.g., Wisotzki et al. 1993; Schechter et al. 1998; Burud et al. 2002; Wisotzki et al. 2003; Metcalf et al. 2003; Chartas et al. 2004). A possible explanation for these differences is that the broad emission line regions of quasars are much larger than the Einstein radii of the microlenses, and the continuum-emitting regions are much smaller than the Einstein radii (Moustakas & Metcalf 2003).

The dependence of temperature on radius in quasar accretion disks also leads to size-dependent effects. Since the disk is cooler far from the center than it is near the central black hole, the disk will have a larger effective radius when observed at long wavelengths than it will when observed at short wavelengths (Vakulik et al. 2003). At long wavelengths, therefore, we expect the magnitude variations due to microlensing to be suppressed. The Shakura-Sunyaev accretion disk model that we use (Section 2.4) incorporates the temperature profile of the disk so that we can study the effects on microlensing fluctuations of varying wavelength and source size. Besides using photometric observations of microlensing, it has also been suggested that astrometric observations, looking for small shifts in image positions due to microlensing, could constrain the sizes of quasars at different wavelengths (Lewis & Ibata 1998; Treier & Wambsganss 2004).

If we describe the size of a source by its half-light radius ( $r_{1/2}$ ), the radius at which half of the light is interior to the radius and half of it is outside, then we can construct different source models with the same half-light radii but with their brightness distributed in the source plane in different ways. We will refer to this distribution of brightness as the “shape” of the brightness profile. Note that all of the source models we consider here are circularly symmetric, so “shape” does not refer to the shape of the contours of constant brightness in the source plane, but rather how the spacing of those contours varies with radius.

The question we would like to address is this: for sources with the same size, as determined by the half-light radius, to what extent does the shape of each source influence the fluctuations due to microlensing of the source? The answer to this question tells us how important the shape of the source brightness profile is to observations and models of microlensing.

Agol & Krolik (1999) and Wyithe et al. (2000b) have also looked at the connection between source properties and microlensing, but their studies use a large number of parameters for the disk models and focus on light curves and caustic-crossing events. Our models have fewer parameters while still covering a wide range of disk shapes, and our main tool for analyzing the effect on microlensing fluctuations is the magnification histogram.

## 2. ACCRETION DISK MODELS

To study the effects of the shape of a source brightness profile on microlensing fluctuations, we use a variety of highly idealized accretion disk models with different shapes to model the source quasar. The first three models (Sections 2.1 to 2.3) are adopted not because they are necessarily realistic, but because they are mathematically simple and span

a wide range of possibilities. The fourth model (Section 2.4), while still an idealization, is physically motivated.

## 2.1. Gaussian Disks

One common type of accretion disk model is a circular two-dimensional Gaussian (e.g., Wyithe et al. 2002). The surface brightness profile (with units of  $\text{erg s}^{-1} \text{cm}^{-2} \text{sr}^{-1}$ ) can be written

$$G(r) = F \frac{D_S^2}{2\pi\sigma^2} e^{-r^2/2\sigma^2}, \quad (1)$$

where  $F$  is the total disk flux at Earth (with units of  $\text{erg s}^{-1} \text{cm}^{-2}$ ),  $D_S$  is the distance from Earth to the quasar,  $r$  is the radius in the source plane from the center of the disk, and  $\sigma$  is the width of the Gaussian (with units of length, measured in the source plane).

## 2.2. Uniform Disks

Even less realistic than the Gaussian disk, a uniform disk is the simplest disk model imaginable. The uniform disk model has a surface brightness of  $FD_S^2/(\pi R^2)$  for radii  $0 < r < R$  (where  $F$  is the total flux at Earth from the disk and  $D_S$  is the distance to the quasar), and is zero for  $r > R$ .

## 2.3. Cones

The “cone” disk model is peaked at the center, and decreases linearly with increasing radius until it reaches zero at a radius  $R$ , outside of which the model is zero everywhere. The surface brightness profile is

$$C(r) = F \frac{3D_S^2}{\pi R^2} \left(1 - \frac{r}{R}\right), \quad r < R, \quad (2)$$

where  $F$  is the total flux at Earth from the disk,  $D_S$  is the distance to the quasar, and  $r$  is the radius from the center.

## 2.4. Shakura-Sunyaev Disks

The last accretion disk model we consider is a thin static disk, viewed face-on, with a two-dimensional brightness profile determined by the temperature at each part of the

disk. Though more complicated than the previous models, it is still simpler than the similar thermal disk models used by Agol & Krolik (1999) and Wyithe et al. (2000b). Many of the results we present in Section 4 use this disk model.

We begin with a temperature-radius relation for the disk adapted from Shakura & Sunyaev (1973):

$$T(r) = 2.049 T_0 \left( \frac{r_{in}}{r} \right)^{3/4} \left( 1 - \sqrt{\frac{r_{in}}{r}} \right)^{1/4}, \quad (3)$$

where  $T_0$  is the peak disk temperature, and  $r_{in}$  is the radius of the inner edge of the accretion disk, which we take to be the radius of the innermost stable circular orbit around the central Schwarzschild black hole. Thus,  $r_{in}$  depends on the black hole mass.

We assume that the disk radiates as a black body with a monochromatic specific intensity  $B_\lambda(T)$  that depends on the temperature, and therefore on the radius. (All wavelengths are assumed to be in the quasar frame, so to compare with wavelengths in the observer's frame the quasar's redshift must be accounted for.) Using Equation (3), we can write the specific intensity as a function of radius:

$$B_\lambda(r) = \frac{2hc^2}{\lambda^5} \left\{ \exp \left[ 0.488 \frac{hc}{\lambda k T_0} \left( \frac{r}{r_{in}} \right)^{3/4} \left( 1 - \sqrt{\frac{r_{in}}{r}} \right)^{-1/4} \right] - 1 \right\}^{-1}. \quad (4)$$

It is convenient to use dimensionless variables for the parameters, so we define a dimensionless wavelength,  $x$ , and a dimensionless radius,  $s$ :

$$x \equiv \frac{kT_0}{hc} \lambda, \quad s \equiv \frac{r}{r_{in}}, \quad (5)$$

which makes the specific intensity

$$B_x(s) = \frac{a}{x^5} \left\{ \exp \left[ \frac{0.488}{x} \left( \frac{s^3}{1 - s^{-1/2}} \right)^{1/4} \right] - 1 \right\}^{-1}, \quad (6)$$

where we define  $a \equiv 2r_{in}^2 h^{-3} c^{-2} (kT_0)^4$ . For the maximum disk temperature  $T_0$  (at  $r = 1.36r_{in}$ ), the peak of  $B_x(s)$  is at  $x_0 = 0.2014$ .

Since the disk radiates at cooler temperatures with increasing distance from the center, observations at different wavelengths will detect different parts of the disk (Wambsgaass & Paczyński 1991; Gould & Miralda-Escudé 1997). To take the wavelength dependence into account, we define a set of filters associated with specific ranges of the dimensionless wavelength  $x$ . The filter numbers increase with increasing wavelength, with filter 0 centered at  $x = x_0$ . The ranges of  $x$  are chosen so that the filters span the space of wavelengths

without overlapping (that is,  $x_{i,max} = x_{i+1,min}$  where  $x_{i,min}$  and  $x_{i,max}$  are the minimum and maximum wavelengths for filter  $i$ ). We assume that each filter transmits 100% of the light in its wavelength range. The filters have constant  $\Delta(\log x) = \Delta x/x_i = 1/5$ , so

$$x_i \approx e^{0.2i-1.6025}, \quad (7)$$

where  $x_i$  is the central wavelength of filter  $i$ .

To create a model of the disk as it would be seen through a particular filter  $i$ , we integrate the monochromatic specific intensity over the wavelengths included in the filter:<sup>1</sup>

$$B_i(s) = \int_{x_{i,min}}^{x_{i,max}} B_x(s) dx. \quad (8)$$

This function  $B_i(s)$ , with units of  $\text{erg s}^{-1} \text{cm}^{-2} \text{sr}^{-1}$ , serves the same purpose for the Shakura-Sunyaev model as  $G(r)$  and  $C(r)$  do for the Gaussian and cone models in the previous sections, except that we use a dimensionless radius as the independent variable and there is a different function for each filter. We can put  $B_i(s)$  in a form similar to the surface brightness profiles of the other disk models if we define the total flux at Earth from the disk in filter  $i$ ,

$$F_i \equiv \frac{2\pi r_{in}^2}{D_S^2} \int_1^\infty B_i(s) s ds, \quad (9)$$

and the normalized surface brightness,

$$b_i(s) \equiv \frac{B_i(s)}{2\pi \int_1^\infty B_i(s) s ds}. \quad (10)$$

Then we can write the Shakura-Sunyaev disk surface brightness as

$$B_i(s) = F_i \frac{D_S^2}{r_{in}^2} b_i(s). \quad (11)$$

Radial surface brightness profiles in four filters are shown in Figure 1.

The Shakura-Sunyaev disk model that we end up with depends on two parameters:  $r_{in}$ , the innermost radius of the disk, and  $i$ , the filter number. The temperature  $T_0$  only determines the relation between  $\lambda$  and  $x$ .

---

<sup>1</sup>For narrow filters, the wavelength across a single filter can be treated as a constant,  $x_i$ , as in Kochanek (2004). This eliminates the need to do the integral in Equation (8), since  $B_i(s) \approx B_{x_i}(s)$ . Note, however, that in Kochanek (2004), the factor of  $(1 - \sqrt{r_{in}/r})^{1/4}$  in Equation (3) is neglected, so those disk models differ significantly from ours for  $r \sim r_{in}$ .

## 2.5. Other Models

Our Shakura-Sunyaev disk model is similar to the thin accretion disk models used by Agol & Krolik (1999) and Jaroszyński et al. (1992). Those models are more complicated, however, as they include rotating black holes, tilted disks, and relativistic effects. Microlensing simulations with nonthermal models have also been considered (Rauch & Blandford 1991), but we do not include such models in this study.

## 3. MAGNIFICATION MAPS

The effect of microlenses on the total macroimage flux may be represented by a magnification map in the source plane, where the value at each point of the map is equal to the magnification of the source at that point, relative to the average macroimage magnification (Kayser et al. 1986; Paczyński 1986; Wambsganss 1990; Wambsganss et al. 1990b). The microlensing light curve of a point source can be found by tracing a path across the magnification map (e.g., Paczyński 1986; Wambsganss et al. 1990b; Kochanek 2004). For an extended source, we must first convolve the source profile with the magnification map to find the magnification due to microlensing at each location in the source plane (e.g., Wyithe et al. 2002).

The maps were made using ray-shooting techniques that send rays from the observer through the lens to the source plane (Kayser et al. 1986; Schneider & Weiss 1987; Wambsganss 1990; Wambsganss et al. 1990a,b; Wambsganss 1999). The maps are 2000 by 2000 pixel arrays with sides of length 100 Einstein radii. We examined two cases typical of the images that might be formed by a galaxy lensing a quasar: a positive parity image (minimum of the time-delay function) with convergence  $\kappa = 0.4$  (all in compact objects), shear  $\gamma = 0.4$ , and theoretical average magnification  $\mu = 5$ ; and a negative parity image (saddle point) with  $\kappa = 0.6$  (again, all in compact objects),  $\gamma = 0.6$ , and  $\mu = -5$ . Magnification maps for each case are shown in Figure 2. The positive parity simulation included 37,469 lenses, and the negative parity simulation included 56,224 lenses.

For each disk model we wished to study, we used the relevant equation from Section 2 to create a 2000 by 2000 pixel array for the disk brightness profile,  $A$ . Let us call the original magnification map  $M$ . By the convolution theorem, we can convolve  $M$  and  $A$  by multiplying their two-dimensional Fourier transforms and then taking the inverse Fourier transform of the product. This produces a new 2000 by 2000 pixel magnification map,

$$C = \text{fft}^{-1} [\text{fft}(M)\text{fft}(A)], \quad (12)$$

where  $\text{fft}$  and  $\text{fft}^{-1}$  stand for the fast Fourier transform and the inverse fast Fourier transform, respectively (e.g., Press et al. 1992). Figure 3 shows two examples of magnification maps from convolutions with Shakura-Sunyaev disk models. Sample light curves for paths through these maps are shown in Figure 4.

The longest wavelengths used in our simulations were chosen so that at least 95% of the total accretion disk intensity would lie within the 2000 by 2000 pixel area of the magnification map. At longer wavelengths, the cooler temperatures of the disk at large radii make the outer regions of the disk more important than in the shorter-wavelength filters. If we use too long a wavelength, a large fraction of the disk intensity spills out of the area of our simulation, making the results inaccurate. The wavelength at which this occurs varies with  $r_{in}$ . Although the cutoff is 95%, for the majority of filters used the fraction of light included in the 2000 by 2000 pixel area is above 99%.

At the short-wavelength end, the cutoff was more arbitrary since the disk profiles and their magnification histograms do not vary much with wavelength beyond a certain point that depends on the value of  $r_{in}$ . We chose to use wavelengths short enough to probe values of the half-light radius (see Section 4.2) close to the inner radius  $r_{in}$  (within one Einstein radius).

## 4. MAGNIFICATION HISTOGRAMS

### 4.1. Histograms of Convolutions with Shakura-Sunyaev Disks

The values in a magnification map are ratios of the macroimage's flux at Earth when the source is at a particular point in the map,  $F(\mathbf{r})$ , to the average macroimage flux,  $\bar{F} = \mu F_s$ , where  $F_s$  is the flux of the unlensed source at Earth. We convert these ratios to magnitude differences,

$$\Delta m(\mathbf{r}) = -2.5 \log_{10} \left( \frac{F(\mathbf{r})}{\bar{F}} \right) \quad (13)$$

and plot a histogram of  $\Delta m$  for the convolution with each disk model, as in Wambsganss (1992). The number of pixels that fall into each bin of  $\Delta m$  is represented as a probability for the macroimage to have a certain magnitude shift by dividing the number of pixels in the bin by the total number of pixels. Histograms of the original magnification maps are shown in Figure 5. Both histograms have two main peaks, typical for images with  $|\mu| = 5$  (Schechter & Wambsganss 2002). A minimum (positive parity) must have at least unit magnification, so the positive parity histogram is cut off at the low-magnification end. At lower magnification, the negative parity histogram has a tail that extends down to  $\Delta m \sim 2 - 3$  mag. The left

peak of each histogram (around  $\Delta m = 1 - 1.5$  mag) is associated with the case of no extra microimage minima, while the right peak around  $\Delta m = 0$  mag is associated with the case of one extra microimage pair (Rauch et al. 1992).

We constructed magnification maps for convolutions with Shakura-Sunyaev disks in several filters with  $r_{in} = 0.2r_E, 0.5r_E, r_E$ , and  $3r_E$ , where  $r_E$  is the microlens Einstein radius. Histograms from some of these maps are shown in Figures 6 and 7. For long wavelengths or large  $r_{in}$ , the histograms are sharply peaked at the average macroimage magnification, and there is little difference between the positive and negative parity cases. These characteristics reflect the loss of detail in the magnification maps for convolutions with disks that have large effective sizes.

## 4.2. Histogram Statistics

Since the surface brightness from disks in different filters falls off with radius at different rates, we can use the half-light radius,  $r_{1/2}$ , as a proxy for wavelength (see Figure 8). For each magnification histogram, we calculated the dispersion (root mean square or rms) and skewness of the data and plotted these statistics against  $r_{1/2}/r_E$ . The results are shown in Figures 9 and 10.

For all disk sizes, the dispersion decreases with  $r_{1/2}/r_E$ . This shows that the effect of microlensing is diminished at longer wavelengths and for larger disks. These trends are expected since the source must be smaller than the microlens Einstein radius for microlensing to play a significant role.

Using the same methods described in Section 4.1, we produced magnification histograms from convolutions with Gaussian disks, uniform disks, and cones. These histograms all have very similar dispersion and skewness as a function of  $r_{1/2}$ ; the dispersion results are shown in Figure 11. From Figures 9 and 10 we see that, for a given value of  $r_{1/2}$ , there is little practical difference between the dispersions of histograms produced with the Gaussian disks and those produced with the Shakura-Sunyaev accretion disk models. This suggests that, to a good approximation, the microlensing fluctuations only depend on  $r_{1/2}$ , and the disk may be modeled with any reasonable surface brightness profile. We examine this claim more quantitatively in the last paragraph of this section.

In the third moment of the histograms, the skewness, we begin to see some greater differences between the Shakura-Sunyaev models and the Gaussian models (lower panels in Figures 9 and 10). However, since skewness is much more difficult to measure with observations than dispersion, these differences may well be unimportant for most applications.

We also used chi-square tests to compare histograms from convolutions with disks that have different shapes and different sizes. Histograms associated with uniform disks require about 10,000 independent observations to distinguish them with 95% confidence from histograms associated with Shakura-Sunyaev disks of the same size; the comparisons between the Gaussian disks or cones and the Shakura-Sunyaev disks need an even greater number of observations, around 40,000. In contrast, the size comparisons tend to require far fewer observations. After examining many sizes of Gaussian disk models and comparing the histograms of their convolutions, we found that to tell apart histograms associated with Gaussian disks that differ in size by  $0.25r_E$  (a quarter of an Einstein radius), it requires 2000 to 4000 independent observations to reach 95% confidence. If we make the difference in size much smaller, the number of observations can be as large as for the shape comparisons (for example, a  $0.05r_E$  size difference in Gaussian disks needs around 40,000 observations for 95% confidence), but in this case the disks with different sizes are intrinsically much more similar than the disks with different shapes, so it is no surprise that the histograms that arise from convolutions with the disks with slightly different sizes are also very similar to each other.

## 5. CONCLUSIONS

We have produced several magnification histograms by convolving source brightness profiles with a variety of shapes and sizes with both positive and negative parity image magnification patterns. These histograms can be thought of as distributions of the probability to observe the macroimage with a certain magnification. We compared histograms associated with disks of different shapes and different sizes by computing moments of the histograms (dispersion and skewness), and by computing chi-square values for pairs of histograms.

By plotting dispersion and skewness against half-light radius (Figures 9 and 10), we discovered that for any particular disk model there is a clear dependence of dispersion and skewness on the half-light radius, but if we compare disk models with different shapes but the same half-light radius, the dispersion and skewness of the associated histograms are only slightly dependent on the shape of the model. This suggests that size differences have a more significant effect on microlensing fluctuations than shape differences do, at least for circular sources.

The chi-square tests confirm this result, showing that the number of observations needed to distinguish sources with differently-shaped brightness profiles but the same size is significantly higher than the amount needed to tell the difference between sources with different sizes but the same shape of the brightness distribution.

This is strong evidence that the dependence of microlensing variability on source shape is far weaker than the dependence on source size. We can model the accretion disk by any circular brightness profile we like—Gaussian disk, uniform disk, or any other well-behaved disk model—and our model will produce the correct results, as long as it is the correct size.

This work was supported by NSF grant AST02-06010.

## REFERENCES

Agol, E., & Krolik, J. 1999, *ApJ*, 524, 49

Burud, I., et al. 2002, *A&A*, 383, 71

Chartas, G., Eracleous, M., Agol, E., & Gallagher, S. C. 2004, *ApJ*, 606, 78

Chiba, M. 2002, *ApJ*, 565, 17

Courbin, F., Saha, P., & Schechter, P. 2002, in *Gravitational Lensing: An Astrophysical Tool*, ed. F. Courbin & D. Minniti (Berlin: Springer), 1

Dalal, N., & Kochanek, C. S. 2002, *ApJ*, 572, 25

Gould, A., & Miralda-Escudé, J. 1997, *ApJ*, 483, L13

Irwin, M. J., Webster, R. L., Hewett, P. C., Corrigan, R. T., & Jedrzejewski, R. I. 1989, *AJ*, 98, 1989

Jaroszyński, M., Wambsganss, J., & Paczyński, B. 1992, *ApJ*, 396, L65

Kayser, R., Refsdal, S., & Stabell, R. 1986, *A&A*, 166, 36

Kochanek, C. S. 2004, *ApJ*, 605, 58

Lewis, G. F., & Ibata, R. A. 1998, *ApJ*, 501, 478

Metcalf, R. B., & Madau, P. 2001, *ApJ*, 563, 9

Metcalf, R. B., Moustakas, L. A., Bunker, A. J., & Parry, I. R. 2004, *ApJ*, 607, 43

Moustakas, L. A., & Metcalf, R. B. 2003, *MNRAS*, 339, 607

Paczyński, B. 1986, *ApJ*, 301, 503

Press, W. H., Teukolsky, S. A., Vetterling, W. T., & Flannery, B. P. 1992, *Numerical Recipes in C* (2nd ed.; Cambridge: Cambridge University Press)

Rauch, K. P., & Blandford, R. D. 1991, *ApJ*, 381, L39

Rauch, K. P., Mao, S., Wambsganss, J., & Paczyński, B. 1992, *ApJ*, 386, 30

Refsdal, S., & Stabell, R. 1997, *A&A*, 325, 877

Schechter, P. L., Gregg, M. D., Becker, R. H., Helfand, D. J., & White, R. L. 1998, AJ, 115, 1371

Schechter, P. L., & Wambsganss, J. 2002, ApJ, 580, 685

Schechter, P. L., et al. 2003, ApJ, 584, 657

Schneider, P., & Weiss, A. 1987, A&A, 171, 49

Shakura, N. I., & Sunyaev, R. A. 1973, A&A, 24, 337

Shalyapin, V. N., Goicoechea, L. J., Alcalde, D., Mediavilla, E., Muñoz, J. A., & Gil-Merino, R. 2002, ApJ, 579, 127

Treyer, M., & Wambsganss, J. 2004, A&A, 416, 19

Vakulik, V. G., et al. 2004, A&A, 420, 447

Wambsganss, J. 1990, Ph.D. thesis, Ludwig-Maximilians-Universität, München, available as MPA550, Max-Planck-Institut für Astrophysik

Wambsganss, J. 1992, ApJ, 386, 19

Wambsganss, J. 1999, J. Comput. Appl. Math., 109, 353

Wambsganss, J., & Paczyński, B. 1991, AJ, 102, 864

Wambsganss, J., Paczyński, B., & Katz, N. 1990a, ApJ, 352, 407

Wambsganss, J., Schneider, P., & Paczyński, B. 1990b, ApJ, 358, L33

Wisotzki, L., Becker, T., Christensen, L., Helms, A., Jahnke, K., Kelz, A., Roth, M. M., & Sanchez, S. F. 2003, A&A, 408, 455

Wisotzki, L., Koehler, T., Kayser, R., & Reimers, D. 1993, A&A, 278, L15

Witt, H. J., Mao, S., & Schechter, P. L. 1995, ApJ, 443, 18

Woźniak, P. R., Alard, C., Udalski, A., Szymański, M., Kubiak, M., Pietrzyński, G., Zebruń, K. 2000a, ApJ, 529, 88

Woźniak, P. R., Udalski, A., Szymański, M., Kubiak, M., Pietrzyński, G., Soszyński, I., & Zebruń, K. 2000b, ApJ, 540, L65

Wyithe, J. S. B., Agol, E., & Fluke, C. J. 2002, MNRAS, 331, 1041

Wyithe, J. S. B., Webster, R. L., & Turner, E. L. 2000a, MNRAS, 318, 762

Wyithe, J. S. B., Webster, R. L., Turner, E. L., & Agol, E. 2000b, MNRAS, 318, 1105

Yonehara, A. 2001, ApJ, 548, L127

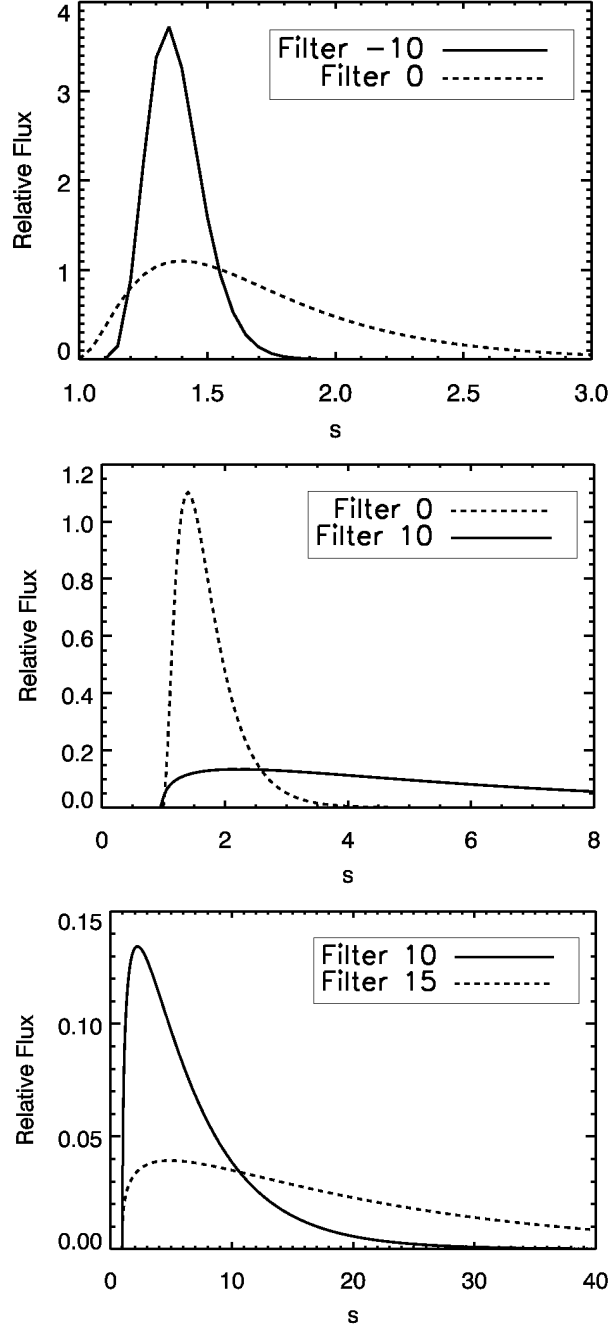


Fig. 1.— Radial surface brightness distributions ( $2\pi s B_i(s)$ ) for an  $r_{in} = 0.2r_E$  Shakura-Sunyaev disk model in four filters, with central dimensionless wavelengths  $x_{-10} = 0.0271$ ,  $x_0 = 0.2014$ ,  $x_{10} = 1.498$ , and  $x_{15} = 4.086$ . The vertical axis is normalized so that the integrated surface brightness equals unity.

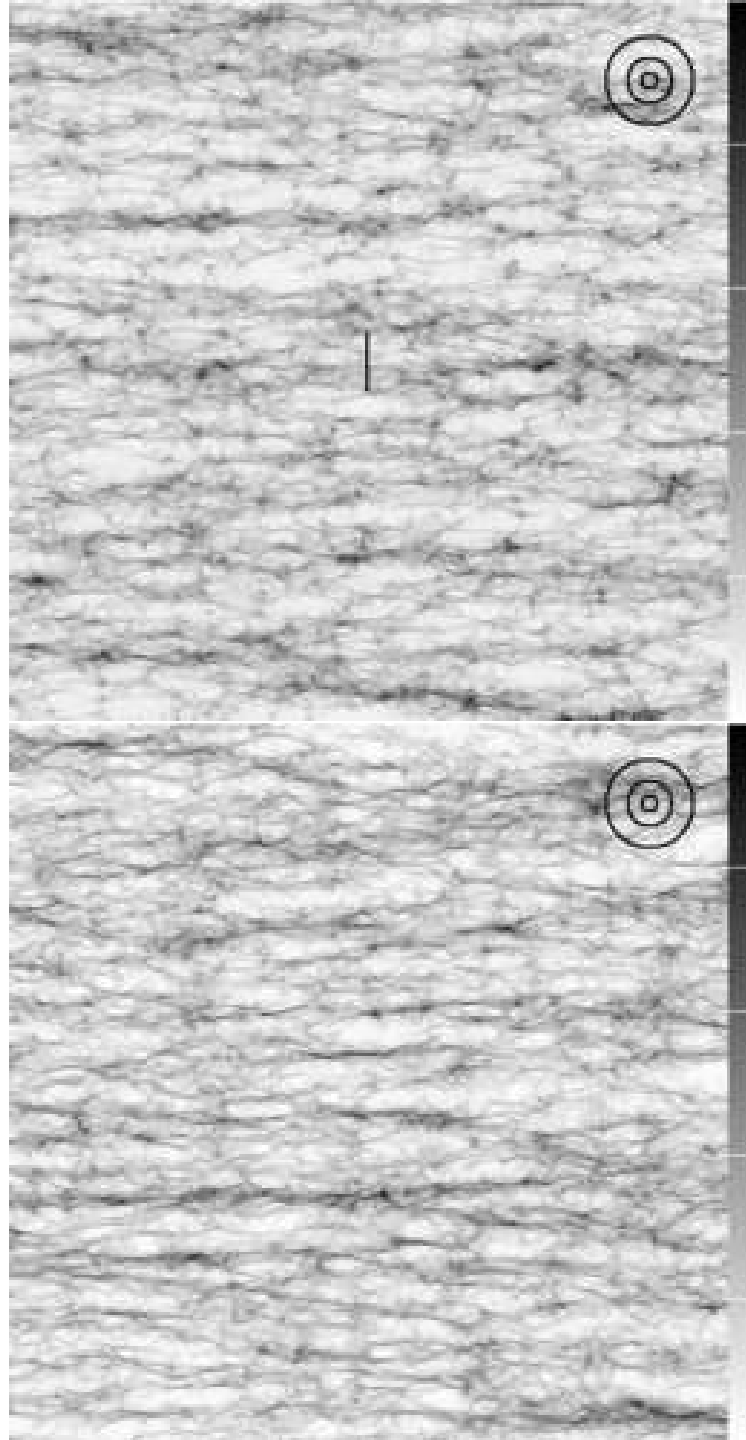


Fig. 2.— Magnification maps in the source plane for a positive parity image with  $\kappa = \gamma = 0.4$  (top) and a negative parity image with  $\kappa = \gamma = 0.6$  (bottom). The length of each side is 100 Einstein radii. The white lines on the greyscale bar correspond to magnifications that are 1, 2, 3, and 4 times the average macroimage magnification. Dark regions have greater magnification than light regions. The black circles have radii of 1, 3, and 6 Einstein radii for comparison with the Shakura-Sunyaev disk models. The black vertical line in the top map shows the path used for the light curves in Figure 4.

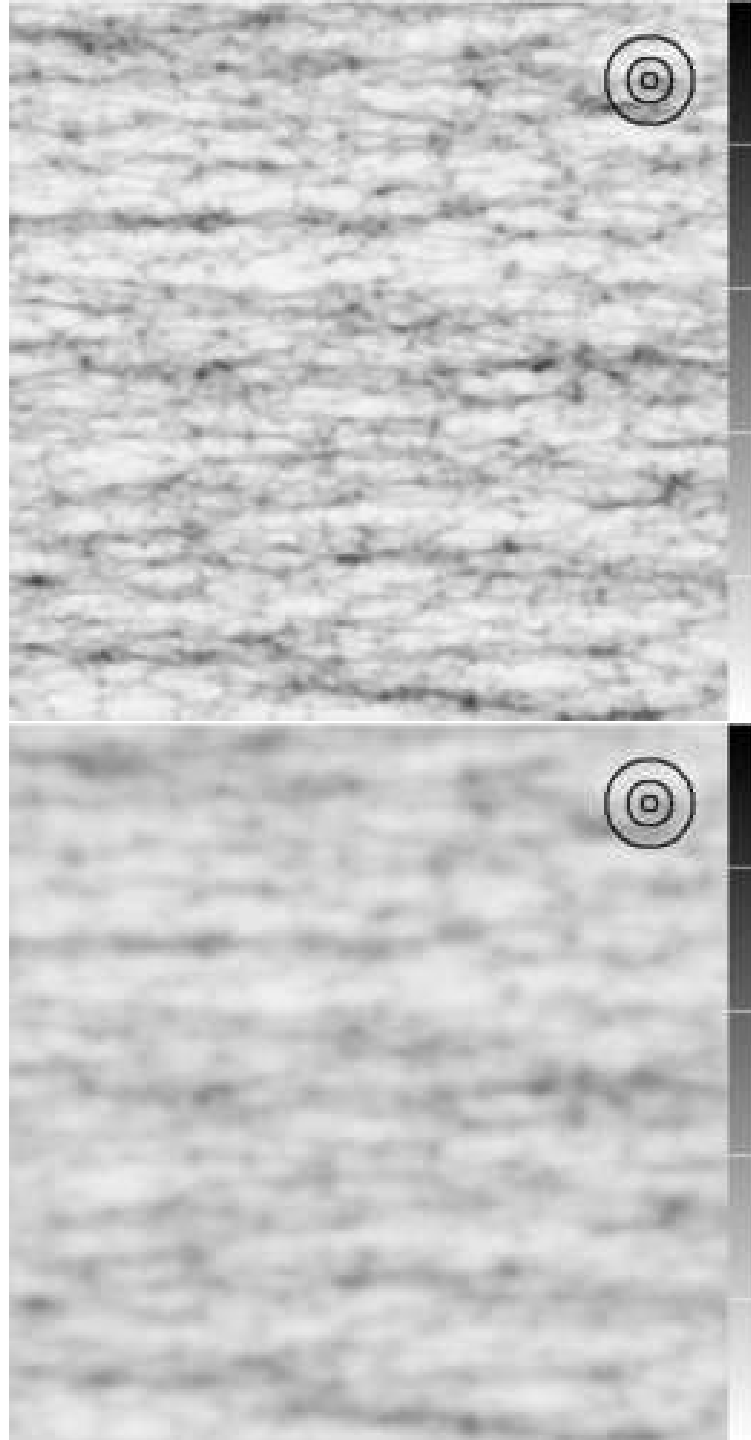


Fig. 3.— Examples of magnification maps from convolving Shakura-Sunyaev disk profiles with the original positive parity pattern in Figure 2. The innermost radius of each disk is  $r_{in} = 0.2r_E$ . For the top map, the filter is  $i = 0$  with central wavelength  $x_0$ , the wavelength of the peak of the blackbody distribution at the maximum temperature  $T_0$ ; the disk surface brightness peaks around  $r = 1.4r_{in}$  at this wavelength. For the bottom map the filter is  $i = 10$  with central wavelength  $x_{10} = 7.44x_0$ , and the peak surface brightness is approximately at  $r = 2.2r_{in}$ . The scale and the reference circles are the same as in Figure 2.

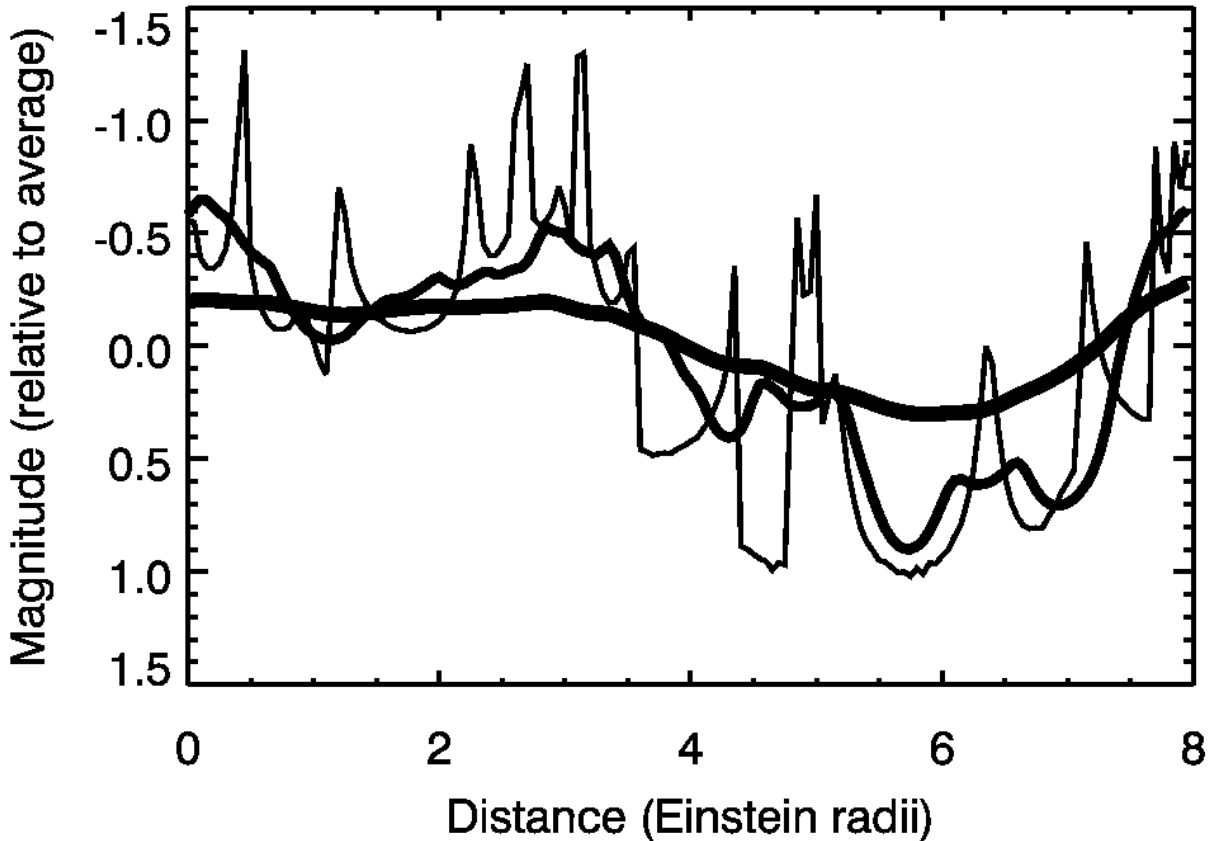


Fig. 4.— Sample light curves from the magnification map on the left in Figure 2 and both maps in Figure 3 ( $\kappa = \gamma = 0.4$ ). The source travels on a vertical path of length 4 Einstein radii in the center of each map (the black line in the top panel of Figure 2). The thin curve is from the unconvolved positive parity map, the medium curve is from the convolution with the disk viewed in the filter associated with the peak surface brightness at the maximum temperature  $T_0$  ( $i = 0$ ), and the thick curve is from the convolution in the filter that is a factor of 7.44 longer in wavelength ( $i = 10$ ).

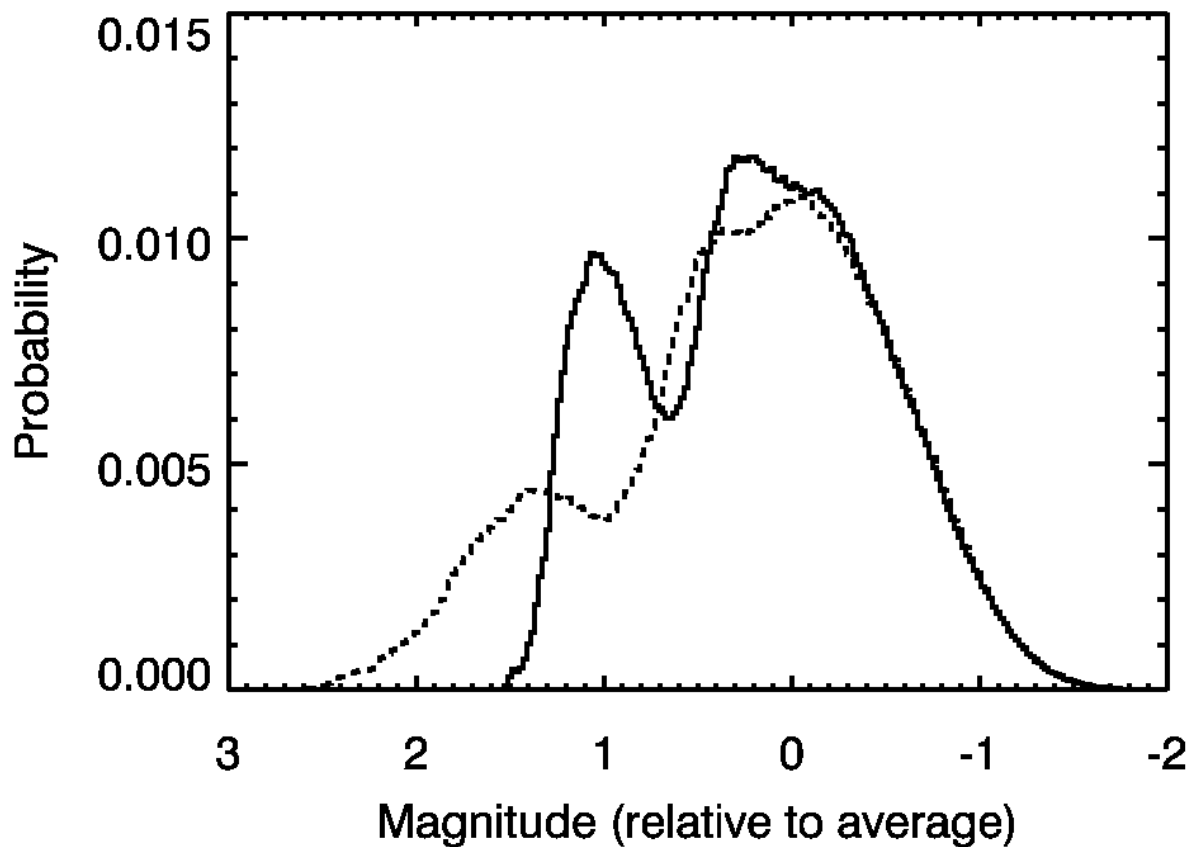


Fig. 5.— Magnification histograms for the unconvolved magnification maps in Figure 2. The solid histogram is from the positive parity image and the dotted one is from the negative parity image. The bin width for each histogram is 0.02 mag.

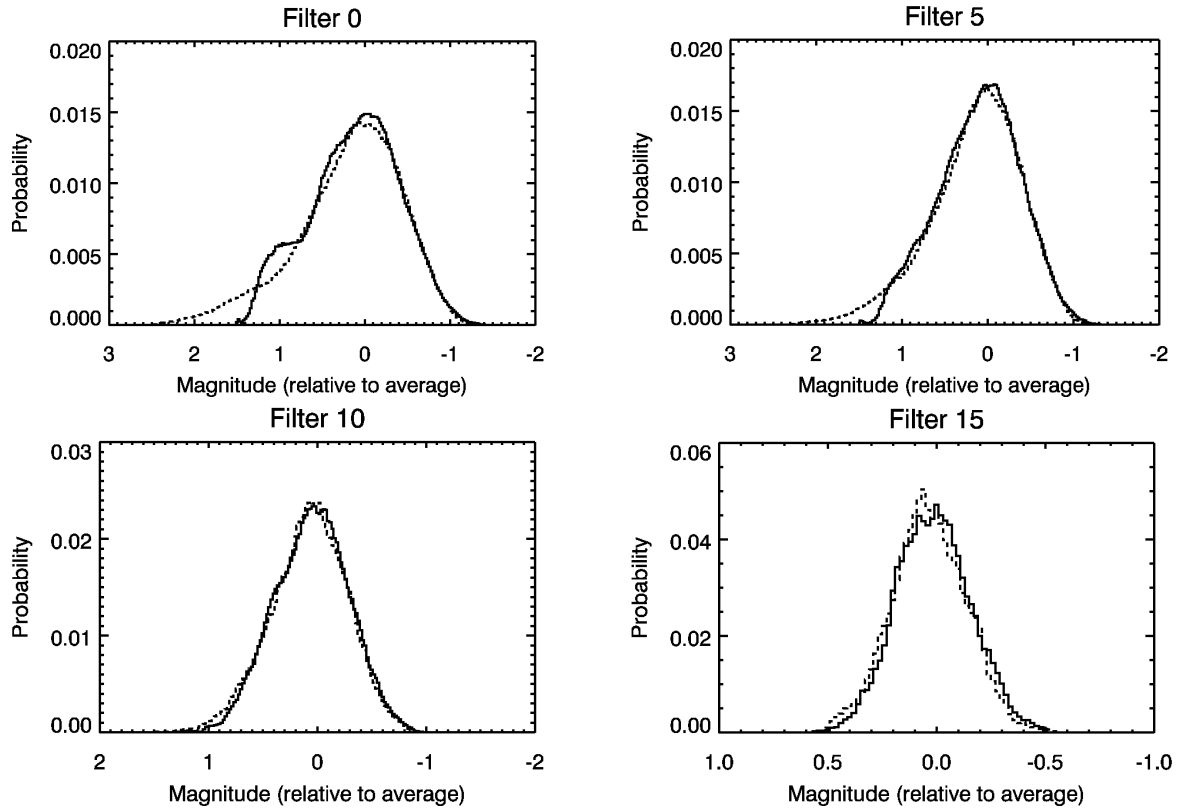


Fig. 6.— Histograms of magnitudes (relative to the magnitude that corresponds to the average macroimage flux at Earth) for convolutions of Shakura-Sunyaev disk profiles with  $r_{in} = 0.2r_E$  in various filters with the positive parity  $\kappa = \gamma = 0.4$  magnification map (solid curves) and the negative parity  $\kappa = \gamma = 0.6$  magnification map (dashed curves). The half-light radii of the disks used as sources are  $0.28r_E$ ,  $0.41r_E$ ,  $1.00r_E$ , and  $3.32r_E$ , respectively. The histograms at shorter wavelengths than that of the filter associated with the peak surface brightness at the maximum temperature  $T_0$  (upper left) are all very similar, so they are not shown here.

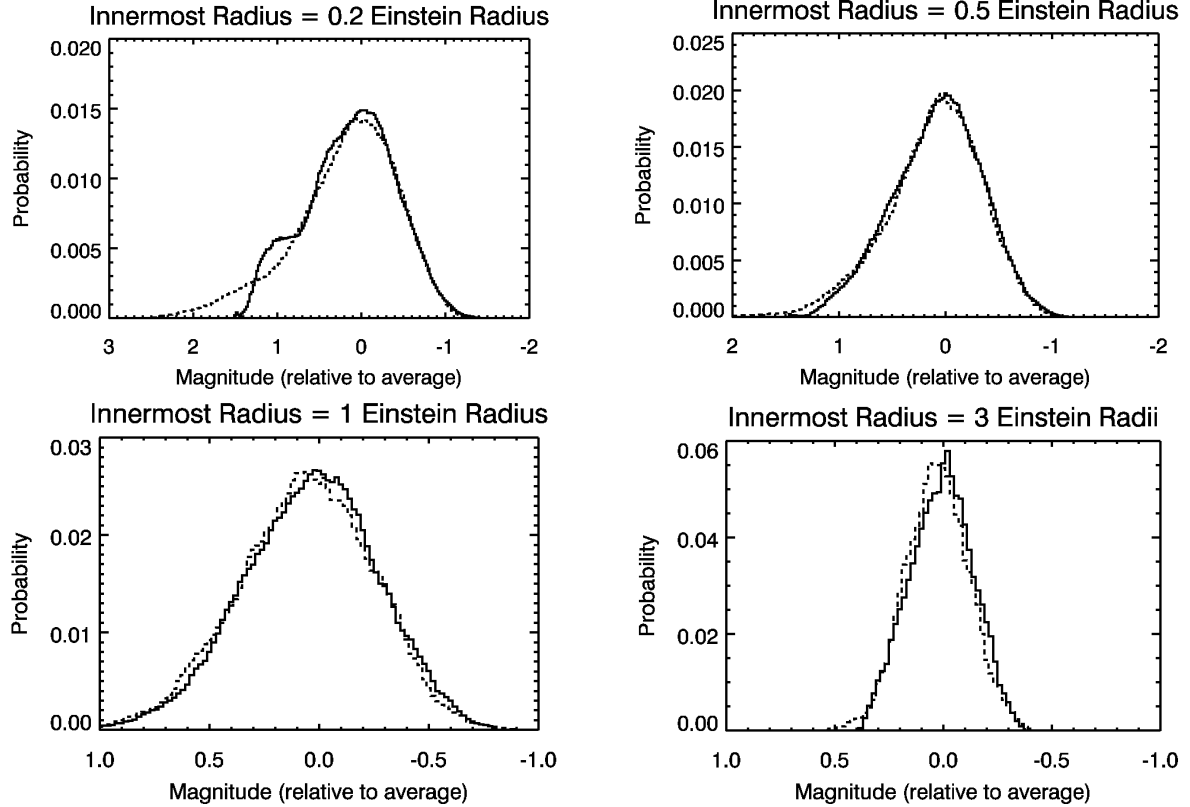


Fig. 7.— Histograms of magnitudes relative to the average for convolutions of Shakura-Sunyaev disk profiles of various sizes in the filter associated with the peak surface brightness at the maximum temperature  $T_0$  ( $i = 0$ ) with the positive parity  $\kappa = \gamma = 0.4$  magnification map (solid curves) and the negative parity  $\kappa = \gamma = 0.6$  magnification map (dashed curves). The half-light radii of the disks used as sources are  $0.28r_E$ ,  $0.77r_E$ ,  $1.58r_E$ , and  $4.84r_E$ , respectively.

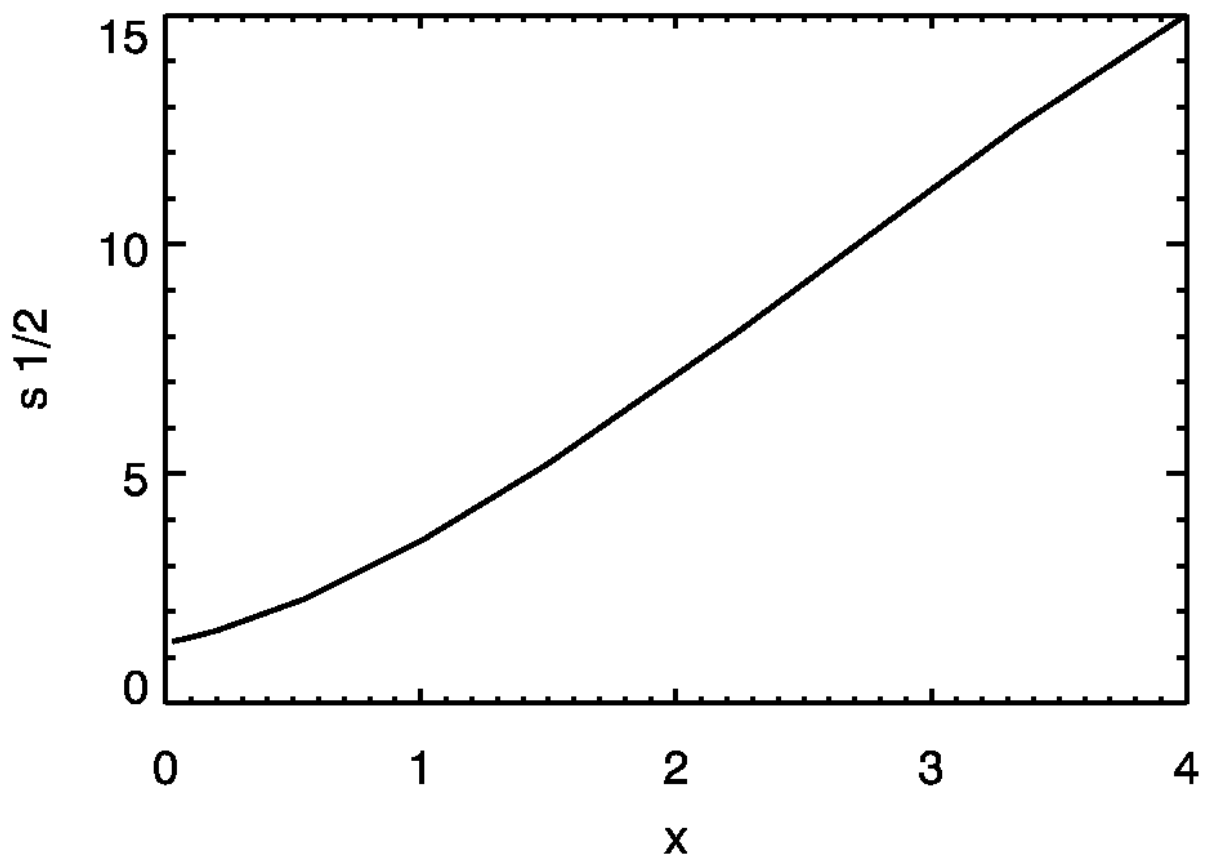


Fig. 8.— Dimensionless half-light radius ( $s_{1/2} = r_{1/2}/r_{in}$ ) versus dimensionless wavelength,  $x$ , for the Shakura-Sunyaev models.

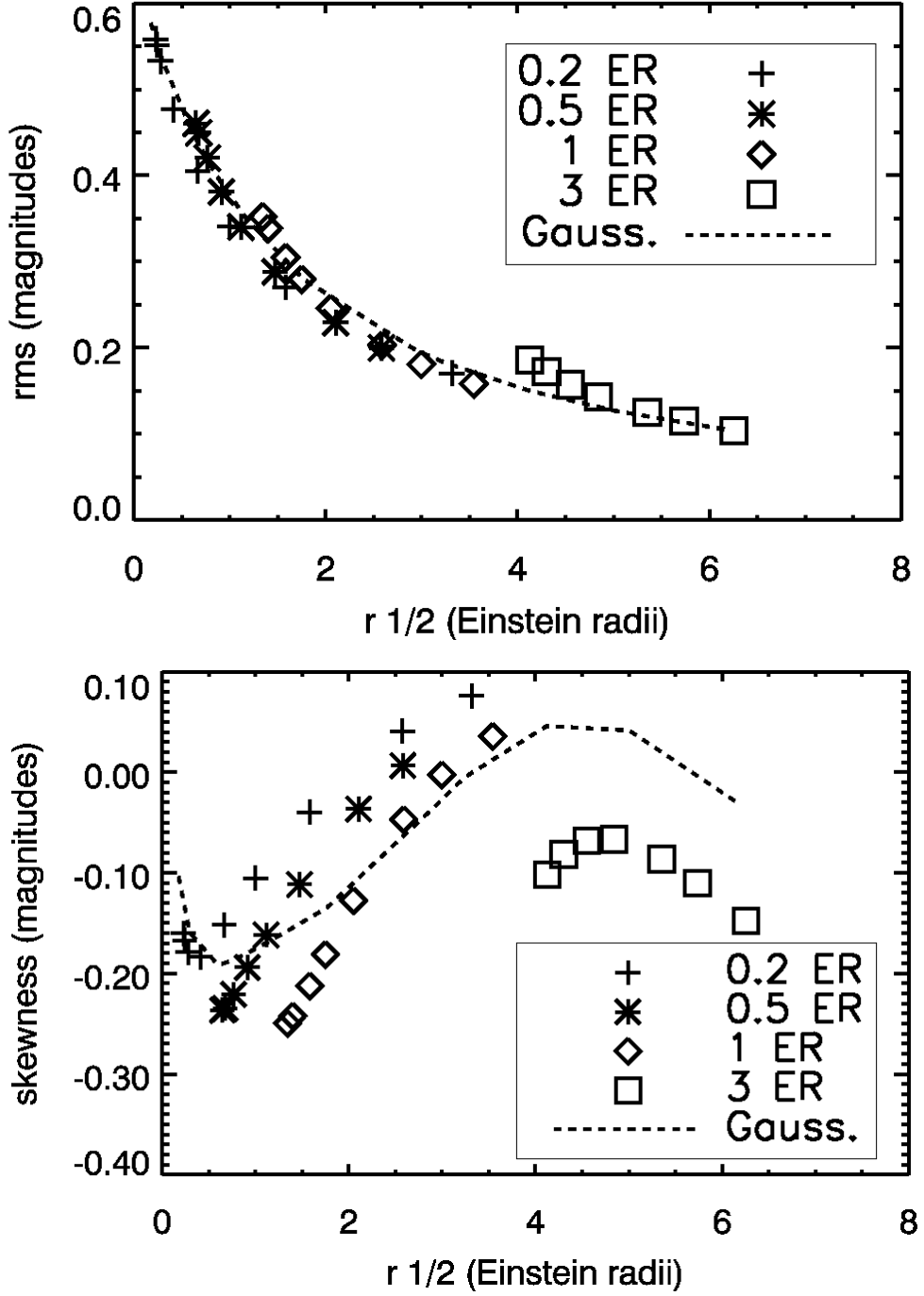


Fig. 9.— Dispersion (rms) and skewness of convolutions of the  $\kappa = \gamma = 0.4$  magnification map with various Shakura-Sunyaev disk profiles. Different plot symbols are used for different values of  $r_{in}$  (given in Einstein radii). Dashed curves for the Gaussian disk models are shown for comparison. Note that negative skewness is associated with a tail toward dimmer (positive) magnitudes.

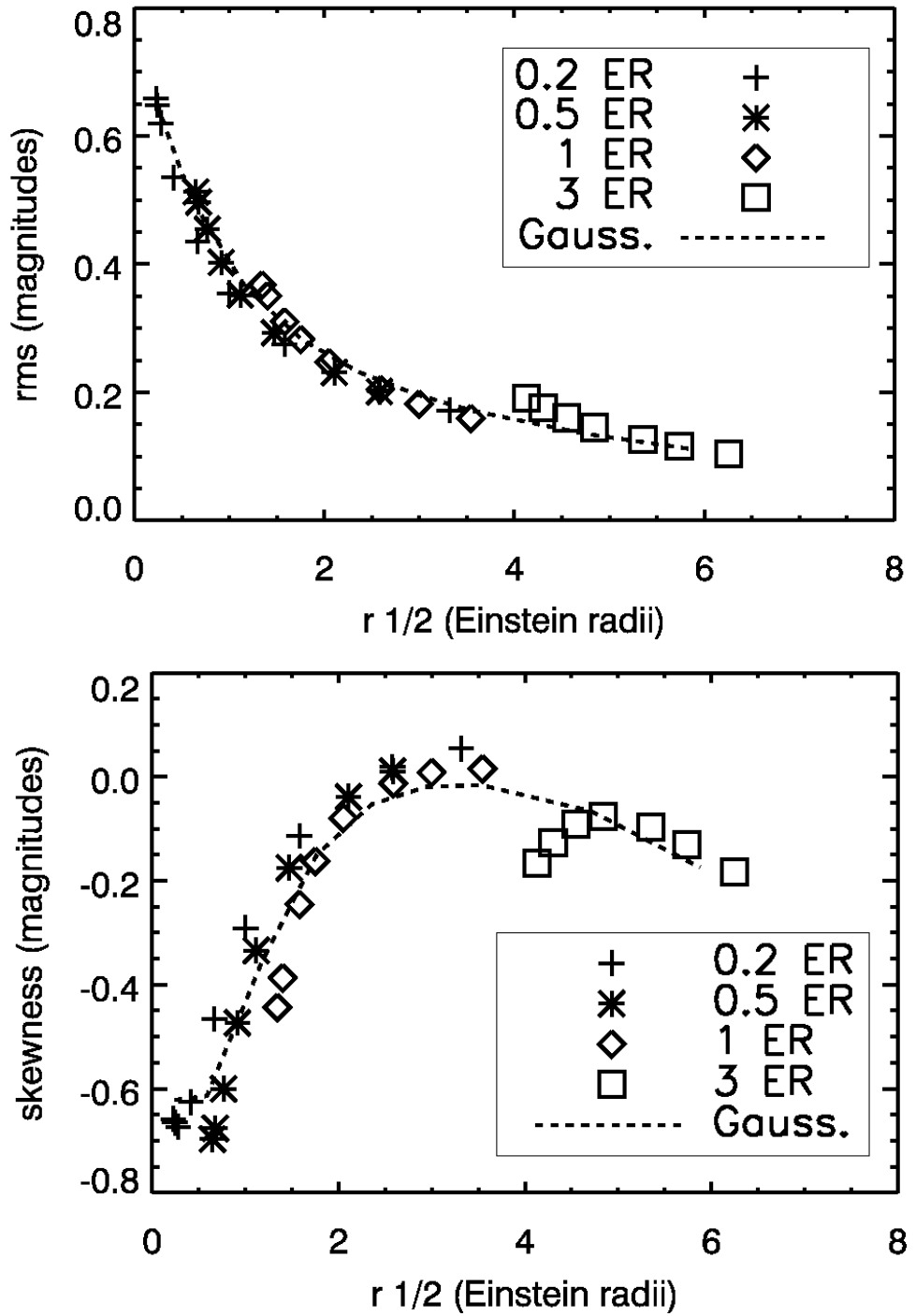


Fig. 10.— Same as Figure 9, here for the negative parity case  $\kappa = \gamma = 0.6$ .

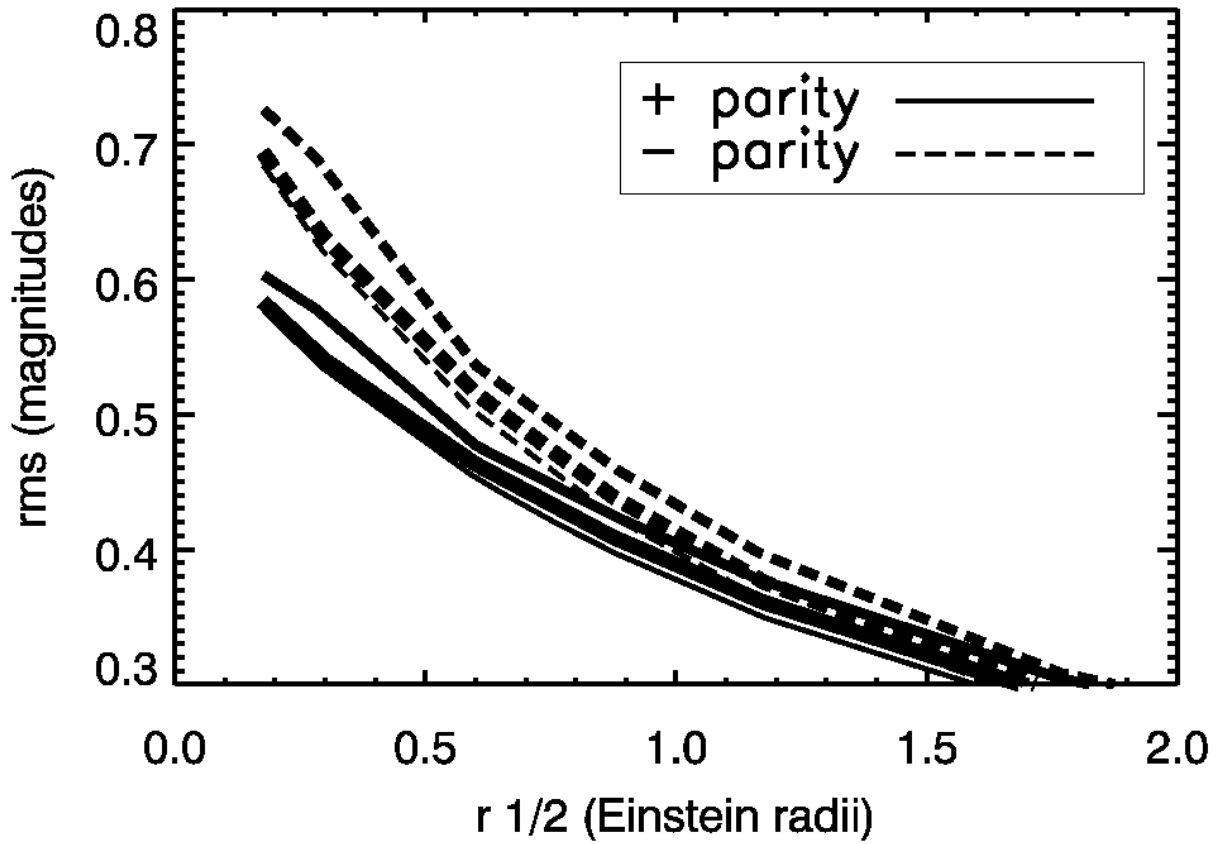


Fig. 11.— Dispersion (rms) of histograms from convolutions of both positive ( $\kappa = \gamma = 0.4$ , solid curves) and negative ( $\kappa = \gamma = 0.6$ , dashed curves) parity magnification maps with Gaussian disks (thin curves), uniform disks (medium), and cones (thick). For values of  $r_{1/2}$  greater than about 2 Einstein radii, the six curves shown here are nearly indistinguishable.